# **Nanoscale**



PAPER View Article Online
View Journal | View Issue



Cite this: Nanoscale, 2018, 10, 19107

# QCM detection of molecule—nanoparticle interactions for ligand shells of varying morphology†

Zachary M. Marsh, D Kayla A. Lantz D and Morgan Stefik D\*

Nanoparticles (NP) have widespread applications from sensing to drug delivery where much behavior is determined by the nature of the surface and the resulting intermolecular interactions with the local environment. Ligand mixtures enable continuously tunable behavior where both the composition and morphology influence molecular interactions. Mixed ligand shells form multiple morphologies ranging from Janus to patchy and stripe-like with varying domain dimensions. Solvent-NP interactions are generally measured by solubility measures alone. Here we develop a quartz crystal microbalance (QCM) approach to more broadly quantify molecule-NP interactions via vapor phase uptake into solid NP-films independent from solvation constraints. The composition and morphology of mixed ligand shells were found to exhibit pronounced non-monotonic behavior that deviated from continuum thermodynamics, highlighting the influence of ligand morphology upon absorption/adsorption. Alkyl and perfluorinated thiols were used as a model case with constant core-size distribution. The ligand morphology was determined by <sup>19</sup>F NMR. Molecule uptake into NPs was measured with five benzene derivatives with varied degree of fluorination. For the cases examined, QCM measurements revealed enhanced uptake for patchy morphologies and suppressed uptake for stripe-like morphologies. These results contrast with insights from solubility measures alone where QCM sometimes identified significant molecular uptake of poor solvents. This QCM method thus provides new insights to molecule-NP interactions independent of the solvation shell.

Received 11th July 2018, Accepted 30th September 2018 DOI: 10.1039/c8nr05605f

rsc.li/nanoscale

### Introduction

Nanoparticles (NPs) have gained widespread interest for a wide array of applications<sup>1</sup> such as chemical and biological sensing,<sup>2</sup> drug delivery for nanomedicine,<sup>3</sup> self-assembly,<sup>4</sup> and removal of contaminants.<sup>5,6</sup> The performance of a NP for an application is largely influenced by its intermolecular interactions with the local environment as determined by the character of the ligand shell. The ligand shell is the ultimate interface of the NP with the outside world and thus governs interactions with other objects. The properties affected by the ligand shell thus range from solubility, to self-assembly, drug delivery, biocompatibility, and targeted molecular uptake. Mixtures of ligands have been shown to enable hybrid beha-

Department of Chemistry and Biochemistry, University of South Carolina, Columbia, SC 29208, USA. E-mail: morgan@stefikgroup.com

 $\dagger$  Electronic supplementary information (ESI) available: NMR and synthetic scheme of the PFOT ligand; example of UV-Vis and NMR with internal standard; example  $^{19}F$  NMR spectra; complete solvent molecule vapor series for all NPs; Tables S1–4 reporting NP size, ligand density,  $^{19}F$  NMR values, and raw QCM molecule uptake data. See DOI: 10.1039/c8nr05605f

viors, *e.g.* NPs with extensive hydrophobic or fluorine content can exhibit solubility in water and other aqueous media.<sup>7,8</sup>

The morphology of mixed ligand shells also significantly modifies NP behavior. On flat substrates, 9 ligand mixtures phase separate to reduce the enthalpic interfacial area<sup>10</sup> where the surface tension has a monotonic dependence on the ensemble composition. 11,12 Here, the molecular environment within each phase is identical to the mono-ligand film. Janus NPs are analogously phase separated with ligand domains on opposite sides of each NP, exhibiting a monotonic continuum of behavior<sup>13</sup> principally corresponding to the ensemble of two mono-ligand environments. Due to high curvature, mixed ligand NPs can also exhibit patchy and stripe-like ligand morphologies when coupled with appropriate pairs of ligands having different length. 14 The lowest free-energy configuration can promote mixed ligand interfaces to increase conformational entropy of the longer ligand. 15 Here the longer ligands explore additional conformational space when proximal to the shorter ligands. This remarkable entropy-driven ordering is widely documented to occur under specific conditions.<sup>17</sup> Patchy and stripe-like NPs are dominated by the mixed ligand interface and thus exhibit non-monotonic trends in behavior

Paper Nanoscale

where the local molecular environment behaves distinctly from the bulk ensemble. The changes in molecule-NP interactions are not yet predictable a priori and are tedious to measure where each molecule-NP interaction is tested individually, typically with a solubility limit measurement. 18-20 The non-monotonic behavior exhibited by patchy and stripe-like nanoparticles has been explained by a combination of cavitation suppressing selective-solvent uptake or by confinement enhancing solvent uptake into appropriately matched molecular environments.<sup>19</sup> Cavitation and confinement thus work in opposing directions where the balance between the two leads to variable non-monotonic molecule-NP behaviors. 13 For example, a recent report with mixed ligand amphiphilic NPs having 67% hydrophobic ligand were most soluble in polar alcohols and this alcohol solubility was reduced when increasing the hydrophilic ligand content.<sup>19</sup>

NP saturation experiments with different solvents or solvation conditions are widely used to quantify solvent-NP interactions. 21-23 In contrast, more general measurements of molecule-NP interactions do not necessarily require a solvation shell. For example, NP drug loading is a separate criterion from solvation in the delivery medium. Here, we develop a quartz crystal microbalance (QCM) method to quantify molecule-NP interactions via vapor phase uptake into solid NP thin films. QCM has previously been used on NP films to monitor chemiresistence, 24-27 detect various biomaterials, 28-30 and to analyze cellular interactions 31 due to its high sensitivity. The approach uses miniscule NP quantities and can uniquely quantify molecule-NP interactions with nonsolvents. Here we examine a model system consisting of 1.8 nm gold NPs with a variable combination of short fluorophilic ligands and long lipophilic ligands that were expected to form patchy and stripe-like ligand morphologies.<sup>32</sup> The molecule-NP interactions were examined for a systematic series of fluorinated benzene derivatives as a function of NP ligand composition and morphology. Non-monotonic trends in solvent uptake were correlated to the ligand shell morphologies as a function of confinement and cavitation effects.

# Experimental methods

#### **Materials**

Gold trichloride (99.9%) was obtained from Strem Chemical and stored under inert atmosphere.  $\alpha,\alpha,\alpha$ -Trifluorotoluene (≥99%, TFT) and anhydrous iodine lumps (99.99%, under argon) were obtained from BeanTown Chemical. Tetrabutylammonium borohydride (≥98%) and didodecyldimethylammonium borohydride (≥98%) were purchased from TCI America and stored under argon atmosphere before use. Potassium thioacetate (98%), benzene (99%), and 1-dodecane thiol (98%, DDT) were obtained from Alfa Aesar and used as received. 1H,1H,2H,2H-Perfluoro-1-iodooctane iodide (≥95%) and 1,3,5-trifluorobenzene (97%) were obtained from Matrix Scientific and used as received. Hexafluorobenzene (97%), 1,2,4,5-tetrafluorobenzene, and 1,4-difluorobenzene were

obtained from Oakwood Chemical and used as received. Chloroform-D (99.8%) and benzene-D<sub>6</sub> were purchased from Cambridge Isotope Laboratories Inc. and used as received. Toluene ( $\geq$ 99.5%) obtained from Fisher Chemical was subjected to four cycles of freeze-pump-thaw and dried over molecular sieves prior to use.

#### 1H,1H,2H,2H-Perfluoro-1-octanethiol (PFOT) synthesis

In a round bottom flask, potassium thioacetate was combined with 2-(perfluorohexyl)ethyl iodide in a 1.1:1 molar ratio along with THF. A condenser was connected to the flask and the reaction vessel was sealed and subjected to three cycles of freeze-pump-thaw to remove excess oxygen. It was then filled with inert nitrogen gas and heated for 5 h at 50 °C. The product was collected through filtration and the excess THF was removed by evaporation. The crude 1H,1H,2H,2H-perfluorooctyl thioacetate was purified through vacuum distillation at 70 °C, purity and structure was verified with <sup>1</sup>H NMR spectroscopy. To obtain the deprotected thiol the purified thioacetate was added to a flask charged with 90 mL of ethanol and 40 mL of concentrated hydrochloric acid. A condenser was connected to the flask and the reaction vessel was sealed and subjected to three cycles of freeze-pump-thaw to remove dissolved oxygen. The vessel was filled with inert nitrogen gas and the reaction was heated for 13 hours at 90 °C. The crude thiol was extracted three times with 100 mL of hexanes and washed with 100 mL of deionized water and then dried overnight with magnesium sulfate. The magnesium sulfate was removed through filtration and the excess hexanes was removed through evaporation before the crude thiol was purified through vacuum distillation. The final purity and structure was verified using <sup>1</sup>H NMR spectroscopy.

#### Amine-stabilized NP (Am. NP) synthesis

In an inert argon glovebox atmosphere, 90 mg of gold(III) chloride was combined with a 0.1 M didodecyldimethylammonium bromide (DDAB) in toluene surfactant solution in a 125 mL Erlenmeyer flask. The solution was gently stirred until the precursor dissolved turning the solution a dark orange color. To this solution 216 µL of dodecylamine was added while stirring, it was then stirred until the dark orange color turned to a light-yellow. In a separate vessel 300 mg of tetra-n-butylammonium bromide (TBAB) was dissolved in 12 mL of the 0.1 M DDAB stock solution, the TBAB solution was then placed in a syringe. Both the flask and syringe were sealed under argon and taken out of the inert atmosphere. The gold precursor solution was then stirred at 1500 rpm. Once the solution reached 1500 rpm the TBAB solution was injected into the stirring flask, it immediately changed from a light-yellow color to a deep red. The resulting Am. NP solution was immediately used for ligand displacement.

#### Ligand displacement procedure

In a typical procedure, a premade ligand solution containing the desired ratio of DDT/PFOT was injected added to the Am. NPs immediately after synthesis. For mixed ligand NPs, the Nanoscale Paper

premade ligand solution was kept at a 1:1 total thiol:gold molar ratio and the proportion of each ligand in the solution was adjusted based on the desired shell composition. Post injection, the AuNPs were stirred for fifteen minutes at room temperature and then boiled at  $120^{\circ}$  C for 20 min for the thiols to displace the dodecylamine ligands. Post boiling, the NPs were immediately washed six times using four toluene washes and two  $\alpha,\alpha,\alpha$ -trifluorotoluene (TFT) washes to remove excess surfactant and excess ligands. After the washing cycles were complete, the particles were collected by centrifugation from methanol and stored as a powder. The resulting NP batches were termed xF according to the final ligand shell composition, *vide infra*, where the NPs had x mol% PFOT.

#### **NMR** experiments

<sup>1</sup>H NMR experiments were carried out on a Bruker Avance III-HD 300 MHz. <sup>19</sup>F experiments were carried out on a Bruker Avance III-HD 400A MHz NMR. The <sup>1</sup>H chemical shifts are referenced to deuterated chloroform, while <sup>19</sup>F chemical shifts are referenced to TFT. An external reference of CFCl<sub>3</sub> was used to shift-correct the <sup>19</sup>F spectra to ensure correct peak positioning.

NP purity was analyzed using <sup>1</sup>H NMR to determine the presence of excess surfactant and unreacted ligand. A typical procedure involved dissolving 5 mg of NPs in either deuterated chloroform or TFT for the heavily fluorinated particles using ultrasonic agitation. The composition of NP ligand shell was measured after ligand stripping using I2 decomposition. Here, 5 mg of NPs were dissolved in deuterated chloroform before 1-3 mg of metallic iodine was added. The solution was gently mixed at 250 rpm using a shaker until complete dissolution of the iodine occurred. It was then allowed to sit overnight to ensure complete disulfide formation. The black precipitate and iodine was removed, and the disulfides were measured using 128 scans on the <sup>1</sup>H NMR. The ligand morphology was determined using 19F NMR measurements with 5 mg of NPs were dissolved in a mixture of TFT/C<sub>6</sub>D<sub>6</sub> (97/3 wt%). The particles were dispersed with a bath sonicator and were scanned using a 100 ppm window centered at -100 ppm with 256 scans.

#### Small-angle X-ray scattering (SAXS)

X-ray experiments were conducted using a SAXSLAB Ganesha at the South Carolina SAXS Collaborative. A Xenocs GeniX3D microfocus source was used with a Cu target to generate a monochromated beam with a 0.154 nm wavelength. The instrument was calibrated using National Institute of Standards and Technology (NIST) reference material 640c silicon powder with the peak position at  $2\theta$  28.44 where  $2\theta$  is the total scattering angle. A Pilatus 300 K detector (Dectris) was used to collect the two-dimensional (2D) scattering patterns. Solutions were prepared by diluting the NPs to  $\sim$ 1 wt% to avoid structure factor contributions. NP solutions were measured within sealed glass capillaries. A blank sample consisting of a capillary with only toluene/TFT was measured under the same conditions for background subtraction. SAXS

data were acquired for 30 minutes at room temperature with an X-ray flux of 21.4 M photons per second incident upon the sample and a sample-to-detector distance of 425 mm. Data were processed using SAXSGUI and custom MATLAB scripts. The scattering form factor was fitted as a Gaussian number average distribution of hard spheres with a 25% standard deviation, determined by fitting several samples with the statistical spread as an independent variable. This constraint was needed to prevent irrational fit convergence.

#### Vapor swelling chamber

The vapor chamber was built in house using a bubbler mounted in a water bath to maintain constant temperature. A dry air line with a flow controller was plumbed into the bubbler to generate vapor at a fixed rate of 27 mL min<sup>-1</sup>. The same flow was also used as a purge line after bypassing the bubbler. The output line was directed into a large temperature-controlled oven set to 35 °C containing a long copper coil to equilibrate the vapor temperature before directing the gas phase into a 0.2 L glass chamber housing the QCM crystal. The exhaust line was plumbed from the glass chamber into a fume hood. Glass and metal connectors were used as much as possible to eliminate diffusive uptake of solvents into plastics.

#### Quartz crystal microbalance measurements

Quartz crystals with 6 MHz resonance frequency were used. NP films were spin coated at 5000 rpm from 1 wt% solutions onto QCM crystals. The crystal was then measured using a Colnatec Phoenix head and a Colnatec Eon-LT monitor. RC cut QCM crystals were chosen to minimize temperature effects. Each measurement started with a system purge of dry air at the same flow rate of 27 mL min<sup>-1</sup> followed by vapor exposure film reached equilibrium, ranging from 25-50 minutes. Following exposure to each solvent, the crystal was again subjected to a purge to remove physiosorbed solvent and restore the baseline QCM frequency. The changes in QCM resonant frequency were recorded 5 times per second. The frequency decrease corresponding to mass uptake was found to equilibrate with a single exponential decay. All data were measured for at least 1.8 times the fitted time constant (>83% progress towards equilibrium) to yield the equilibrium molecular uptake. The resulting frequency data was analyzed using custom MATLAB R2016b scripts. The changes to QCM resonant frequency were converted to the corresponding mass change using the Z-Match method:

$$\Delta_{\mathrm{m}} = \frac{v_{\mathrm{q}} \cdot \rho_{\mathrm{q}}}{2\pi \cdot z \cdot f_{1}} \cdot \tan^{-1} \left( z \cdot \tan \left( \frac{\pi \cdot (f_{0} - f_{1})}{f_{0}} \right) \right) = \mathrm{g \, cm^{-2}}$$

where  $\Delta_{\rm m}$  is the change in mass (g cm<sup>-2</sup>),  $v_{\rm q}$  is the frequency constant (333 600 cm s<sup>-1</sup>),  $\rho_{\rm q}$  is the density of quartz (2.648 g cm<sup>-1</sup>), Z is the Z-factor (1 for mass loadings less than 10–20% frequency shift),  $f_1$  is the final resonant frequency, and  $f_0$  is the initial resonant frequency. The NP-film mass (g cm<sup>-2</sup>) was determined by using the resonant frequency of the bare QCM as  $f_0$  and the resonant frequency with the NP-film as  $f_1$ . The molecular mass uptake (g cm<sup>-2</sup>) was deter-

mined similarly by using the resonant frequency of the NP-film as  $f_0$  and the resonant frequency with the NP-film under saturated vapor as  $f_1$ . Statistical uncertainty was determined either with repeated measurements or estimated as 10% of the nominal value.

#### Calculation of solvent-NP interaction

**Paper** 

The molecule–NP interaction was compared for each solvent as a function of the NP ligand shell. The molecular uptake for each film was normalized by the NP film mass to yield comparable relative extents of uptake. The ratio of  $(g_{molecule} \ cm^{-2})/(g_{film} \ cm^{-2})$  yielded  $g_{molecule}/g_{film}$ . The vapor pressure was maintained constant for each solvent since the molecular uptake mass  $(g_{molecule})$  is dependent upon vapor pressure.

#### Ligand surface density calculations

The ligand surface density for NPs was determined using a combination of UV-Vis and quantitative  $^1H$  NMR. The concentration of the gold NPs was analyzed using a Shimadzu UV-2450 Spectrometer over an absorbance range of 600 to 400 nm. Samples were prepared at approximately 0.2 mg of NPs per 1 mL solvent and placed in a fused quartz glass cuvette with a 1 cm pathlength. The concentration was calculated using Lambert–Beer law using the absorbance at 508 nm and the extinction coefficient based on the known NP diameter. The extinction coefficients were calculated using the constants k (3.32111) and a (10.80505).

The ligand concentration was quantified after iodine decomposition using  $^1H$  NMR spectroscopy with an internal standard of known concentration. Here the ratio of the internal standard (1,4-difluorobenzene) to the ratio of the  $\alpha$  H1 peaks of each ligand were used to quantify the concentration of each ligand as detailed elsewhere.  $^{34}$  Iodine decomposition was carried out by adding 1–3 mg of metallic iodine to the dispersed NPs, the particles were left to decompose for at least 12 hours to ensure complete disulfide formation leading to a color change from deep red to clear violet. After twelve hours the black precipitate was filtered off and the solution was taken for  $^1H$  NMR analysis.

## Results and discussion

#### Preparation of mixed-ligand NP

A range of mixed ligand NPs were synthesized under conditions expected to form patchy and stripe-like ligand morphologies. The formation of these morphologies are attributed to ligands with different lengths on a NP of suitable curvature, e.g. generally  $\sim 2-8$  nm in diameter.  $^{35,36}$  A recent experimental and computational study examined mixtures of fluorophilic and lipophilic ligands on 2-4 nm gold NPs where the length of the ligands were varied across a wide composition range to determine the impact on ligand morphology.  $^{32}$  Janus regions were observed if the ligands had similar length. The flexible lipophilic ligands needed to be >4-6 carbons longer than the stiff fluorinated ligands to form patchy or stripe-like

morphologies. The morphologies were mapped for patchy (0–30 mol% fluorinated and 60–100 mol% fluorinated) and stripe-like (30–60 mol% fluorinated) morphologies. These prior works<sup>32</sup> suggest that our selection of DDT and PFOT (4 carbon difference) with 1.8 nm diameter Au NPs will yield patchy and stripe-like ligand morphologies.

Mixed ligand NPs were prepared using standard methods. Murray et al.37 developed a method for mixed ligand NPs using a post-synthesis ligand exchange. This process was later expanded to displace weakly bound amine or phosphorous ligands with stronger binding thiol ligands.38 The first stage of a ligand displacement involves competitive binding where molar excess or differential binding strength result in preferential deposition of the new ligand(s). With mixed ligands, the next stage is the evolution of the ligand shell morphology via continuous ligand exchange with the solution. The desorption/ binding rates as well as the chemical dissimilarities establish the timeframe for this process.<sup>39</sup> The NP core size is thus constant and is decoupled from the final ligand chemistry 38,40 (Fig. 1). Our synthesis used a procedure for aminated <5 nm (ref. 40) Au NPs followed by amine displacement with lipophilic DDT and fluorophilic PFOT ligands. The NP behavior followed broad expectations where PFOT-rich NPs precipitated from toluene whereas DDT-rich NPs were toluene

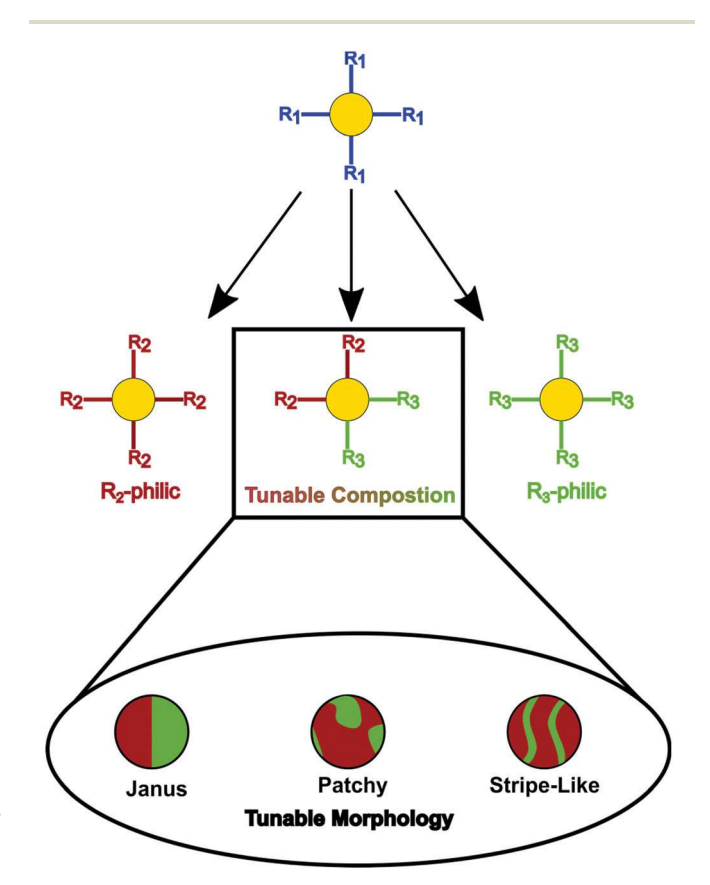


Fig. 1 NPs with mixed ligand shells can have variable composition and ligand morphology. Displacement of weakly bound ligands ( $R_1$ ) with strong binding ligands ( $R_2$ ,  $R_3$ ) yields systematic NP series with constant NP core size distribution and variable ligand shells.

Nanoscale

soluble. SAXS was used to confirm the NP size distributions. Comparison of the Am. NPs to ligand displaced NPs resulted in similar scattering curves with the nearly identical q-positions for local minima and maxima (Fig. 2). Each dataset was well fitted using a hard sphere form factor with a Gaussian size distribution. The results indicated nominal NP diameters from 1.7-2.1 nm, with some minor differences between the

converged fits (Table S1†). Thus, ligand displacement was shown to not significantly alter the NP core size distribution and thus morphology changes are not due to significant size NP changes.

The resulting mixed ligand NPs were rigorously purified before determination of the ligand surface density and composition. The synthesis solution contained a surfactant to improve NP solubility, however residual surfactant would influence subsequent measurements of molecule-NP interactions. The NPs were thus purified with iterative dispersal/precipitation cycles. The solubility of the NPs changed markedly with the cleaning steps as well documented before.41,42 NMR spectra after six wash cycles were without sharp peaks associated with free-ligand or surfactant (Fig. 3). An aliquot of the mixed ligand NPs was then striped of ligands using metallic iodine to improve quantification of the formerly-bound ligand population (Fig. 4). The ratio of bound ligands was fully tunable from 0-100 mol% PFOT with minor deviation from the exchange solution composition (Fig. 5 and Table S2†). A non-convolved internal standard (1,4-difluorobenzene) was included in the same ligand stripping experiments to determine the ligand surface concentration. A fringe benefit of the chosen internal standard is that it also improves NP solubility. Comparison of the ligand concentration to the

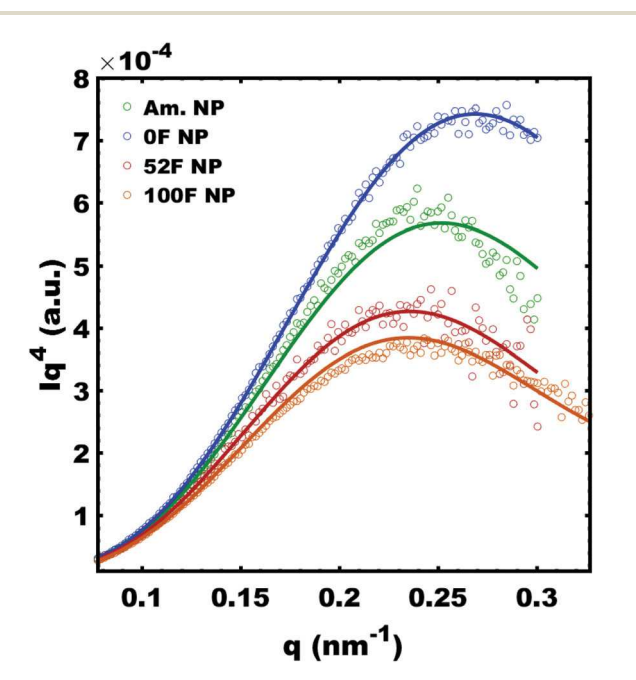


Fig. 2 Porod plots of aminated, OF, 25F, 52F, 100F NP solutions, Data points and best-fit lines are indicated. Scattering data were scaled for clarity.

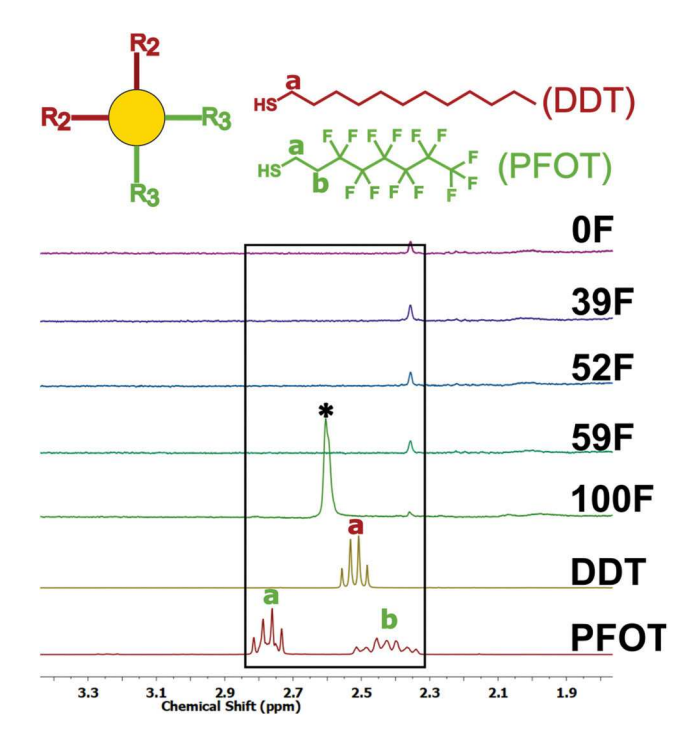


Fig. 3 NMR of the ligated nanoparticles after washing showing the absence of free ligand. Reference spectra for the pure DDT and PFOT thiols are presented. \*TFT added for solubility. The NPs were named by the mol% of PFOT in the DDT/PFOT ligand shells, see Fig. 4.

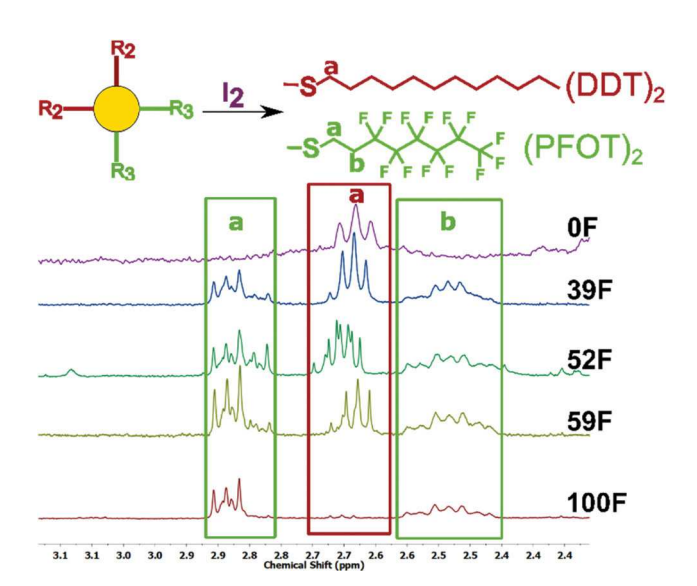


Fig. 4 The NP bound ligand composition was measured by NMR after ligand stripping with iodine, resulting in the corresponding disulfide mixtures.

NP concentration determined by optical absorption experiments yielded the surface ligand density. The ligand surface density for all mixed-ligand NPs examined were within the range of 1-5 # per nm<sup>2</sup>, consistent with similar reports of NPs without detectable free-ligand<sup>34</sup> (Table S2†). A series of puri-

50

**Paper** Nanoscale

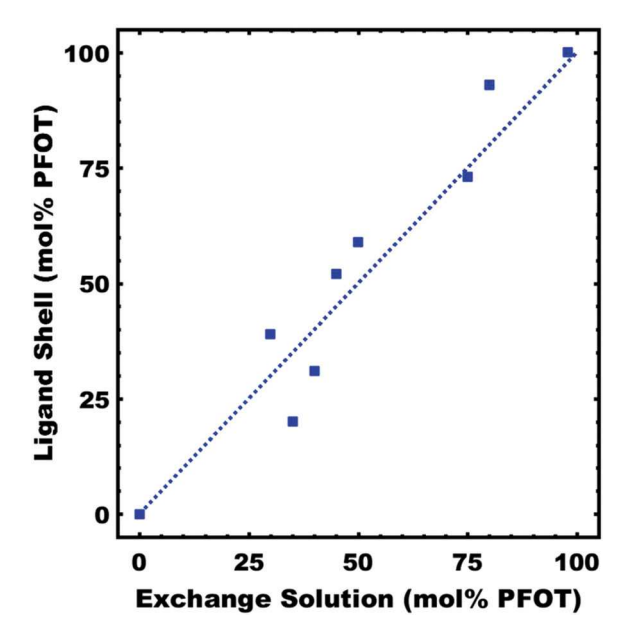


Fig. 5 Correlation of ligand exchange solution composition to the composition of bound ligands on nanoparticle surfaces (DDT and PFOT ligands).

fied DDT/PFOT mixed ligand NPs were thus prepared with constant size distribution.

#### Determination of ligand morphology by <sup>19</sup>F NMR

Numerous methods can determine the morphology of mixed ligand NP shells. Common methods include NMR, 43,44 mass spectroscopy, 45 Microscopy, 46 Scanning Tunneling MALDI-TOF,<sup>39</sup> UV-Vis paired with Cryo-TEM,<sup>47</sup> Electron Spin Resonance,48 Infrared Spectroscopy paired with STM,49 and contact angle measurements.<sup>50</sup> Here we used the method developed by Pasquato et al. to determine the mixed ligand morphology using trends in <sup>19</sup>F NMR chemical shifts. The method was demonstrated with similar fluorophilic/lipophilic ligand mixtures and was supported by computational predictions.32 By using 19F NMR, which has high sensitivity due to the large chemical shift range, small changes in the local environment result in larger chemical shifts. If a ligand is surround by identical neighbors, similar to a mono-ligand film, then the chemical shift is insensitive to composition changes. Interfaces of different ligands have a different chemical shift where the extent of the shift is a weighted average of the local ligand environments. Distinct trends in chemical shift with ligand composition are anticipated for different sequences of ligand morphologies. Linear decays, exponential decays, and sigmoidal decays were previously correlated to random packing, patchy/Janus, and patchy/stripe-like morphologies, respectively. The 19F NMR measurements of both the CF3 group centered near ~80 ppm and the CF2 group centered near ~127 ppm both exhibited sigmoidal trends in chemical shift with ligand composition for the synthesized NP series (Fig. 6). Both curves exhibit similar trends in the chemical

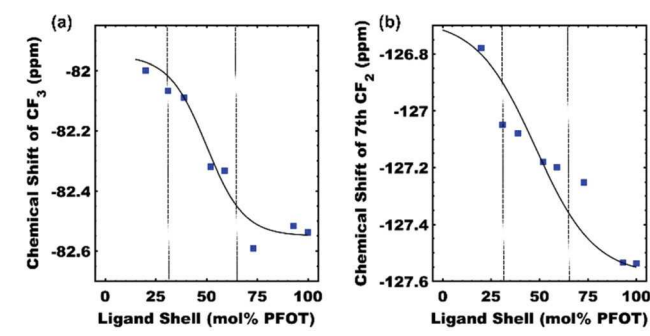


Fig. 6 Trends of  $^{19}$ F NMR chemical shift for  $-CF_3$  (a) and the 7th  $-CF_2$ -(b) on PFOT as a function of NP ligand composition (DDT/PFOT). A sigmoidal guide line is presented. Interpreted transitions in ligand morphology are indicated with dashed drop lines.

shift decay suggesting transition from patchy to stripe-like to patchy morphologies, similar to analogous NP preparations.<sup>32</sup>

#### QCM quantification of molecule-NP interactions

A custom QCM apparatus was constructed to quantify molecule-NP interactions. Each NP-film was prepared directly on a quartz crystal by spin coating NP solutions. The NP-film was subsequently exposed to solvent vapor and the mass uptake was quantified by the shifting resonant frequency of the quartz crystal. An advantage of QCM is rapid real-time feedback with high mass-resolution, the use of minute NP quantities, and the ability to measure molecule uptake without requiring a solvation sphere. Early experiments guided our selection of films that were approximately 60 nm thick or less to minimize diffusion time. This thickness was consistently achieved by using a 1 wt% NP solution and a spin speed of 5000 rpm for an even, thin film on the crystal surface. Slower spin speeds (<2000 rpm) resulted in >100 nm thick films with excessive equilibration times. For typical experiments, the frequency response to vapor was exponential with a time constant that ranged for each film from 8-14 minutes. A typical uptake experiment is shown in Fig. 7b. Comparison of the molecule mass uptake to that of the NP-film thus quantifies the relative extent of uptake. The experiment is easily extendable by examining multiple molecule vapors sequentially (Fig. 7c). Typical experiments yielded 10-35% molecule mass uptake relative to the film mass. Repeated measurements exhibited 2-10% variation of the absolute uptake values, Table S5.† The complete vapor series for each particle composition can be found in the ESI (Fig. S4-11†). The effect of ligand morphology on molecular uptake are presented next by comparison of the QCM response of NPs with different mixed ligand compositions.

## Correlation of ligand morphology to molecule-NP interactions

The simplest approach for series comparisons of molecule-NP interactions is with variable NPs and constant molecule vapor. This eliminates the need to quantify and vary the vapor pressure for direct molecule comparisons.<sup>51</sup> A distinct benefit of our QCM method is the quantification of molecule-NP Nanoscale Paper

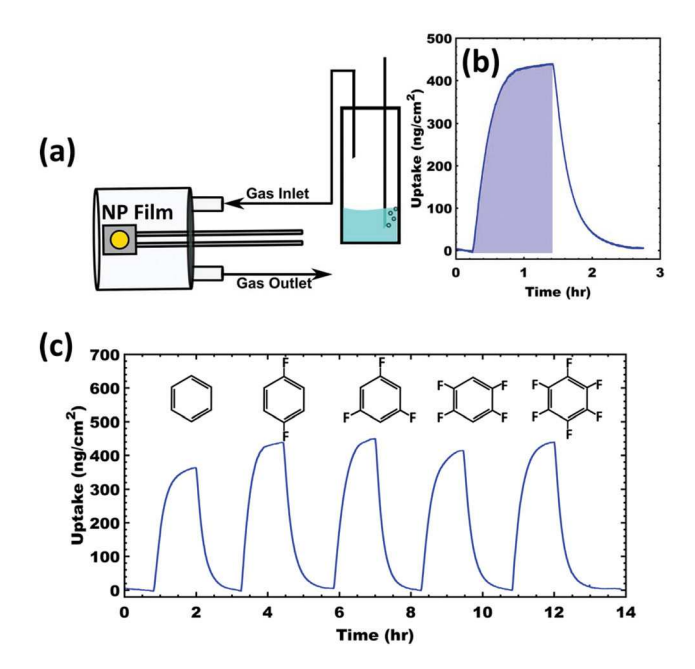


Fig. 7 (a) Scheme of QCM setup with controlled solvent vapor. (b) A characteristic vapor response curve for the OF NP film with 1,4-difluorobenzene where the shaded region represents the solvent uptake. (c) A sequential series of solvent measurements for a OF NP film with benzene, 1,4-difluorobenzene, 1,3,5-trifluorobenzene, 1,2,4,5-tetrafluorobenzene, and hexafluorobenzene vapor, respectively.

interactions for non-solvents. The systematic series of mixed ligand NPs prepared above are ideal candidates for the development and testing of this new QCM based approach to probe for non-monotonic trends in molecule-NP interactions with changes to the ligand composition and thus ligand morphology. Our synthesis strategy notably eliminates the nanoparticle size distribution as a variable by using a ligand exchange strategy. Recent experimental and computational work coupled with our <sup>19</sup>F NMR measurements suggests a sequence of patchy and stripe-like morphologies here.

First, the uptake of benzene vapor was systematically examined using a range of NP surface compositions (Fig. 8). NPs with only DDT ligands up took 15 wt% benzene mass and NPs with only PFOT ligands up took 11 wt% benzene mass. These two extreme points constrain the possible trajectories for monotonic behavior trends to be in intermediate to these two values. The NPs used here with stripe-like morphologies (39-59 mol% PFOT) exhibited reduced solvent uptake relative to the two mono-ligand cases, indicative of molecular cavitation. In contrast, the NPs used here with patchy morphologies (both PFOT-poor and PFOT-rich) exhibited markedly enhanced uptake, indicative of molecular confinement. For example, the 20F NPs up took 28 wt% benzene, a ~2× increase relative to the OF NPs despite the addition of a fluorophile. Clearly, the molecule-NP interaction is sensitive to the character of the ligand morphology. We note that <sup>19</sup>F NMR of 31F was at a transition between patchy and stripe-like morphologies and was thus excluded from discussion of generalized trends due to

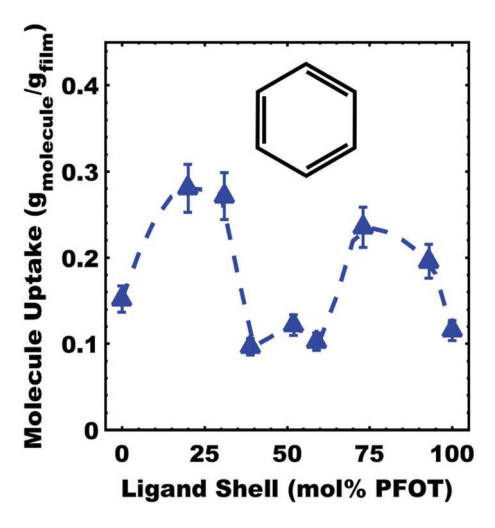


Fig. 8 Mass uptake of benzene vapor in NP films as a function of PFOT: DDT mixed ligand shell composition.

ambiguity. The trends in uptake may be attributed to the nominal dimension of the ligand domains, increasing when transitioning from stripe-like to patchy morphologies. Molecular confinement, e.g. within the gaps between the short and tall ligands, requires that the ligand domains accommodate both the molecule functionality and dimensions. This was rationalized with a confinement argument in a prior study. 19 An interesting feature is that even the 100F NPs with mono-ligand PFOT up took 11 wt% benzene; this interaction of benzene would be missed by solubility measurements alone as the 100F NPs are nearly insoluble in benzene. This marked difference between solubility measurements and QCM solvent uptake exhibit the distinction between molecular uptake and the capability to form a favorable solvation shell. Thus, QCM enables additional insights to quantify molecule-NP interactions independent of solubility.

Next a systematic series of benzene derivatives were examined with variable extent of fluorination to determine the effect on overall molecule-NP interactions. The derivatives included 1,4-difluorobenzene, 1,3,5-trifluorobenzene, 1,2,4,5tetrafluorobenzene, and hexafluorobenzene and were deliberately selected without permanent molecular dipoles. Each solvent was examined across the same series of NP compositions and morphologies as above with benzene (Fig. 9 and Table S3†). Analogous behavior to benzene was found in all cases where (1) relative to the mono-ligand cases, the patchy NPs exhibited enhanced uptake corresponding to confinement effects and (2) relative to the mono-ligand cases, the stripe-like NPs exhibited reduced solvent uptake corresponding to cavitation effects. Similarly, large changes in nanoparticle solubility by 230-250% were reported for minor composition changes of mixed ligand shells from 8-17 mol%. 19 These generalized behaviors for the aromatic molecule series suggests an important role of the relatively constant molecular shape, size, and presence of the aromatic ring. As expected with a like-dis**Paper** 

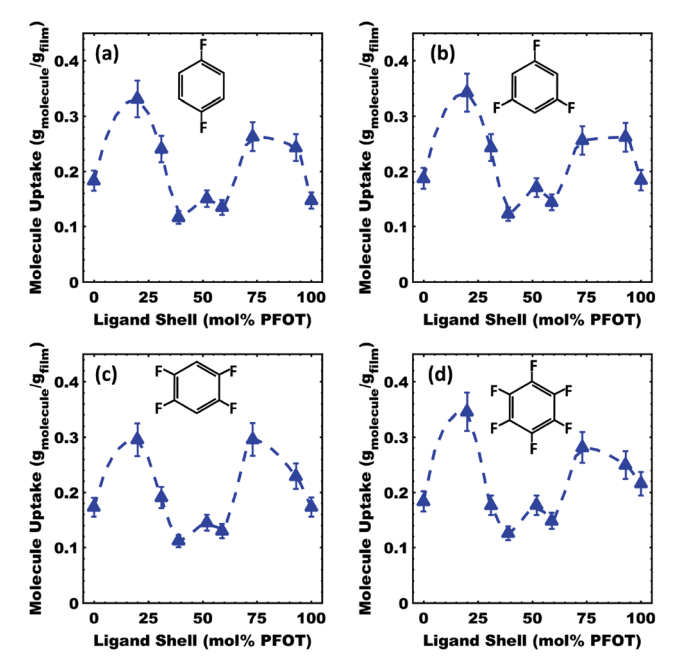


Fig. 9 Mass uptake of solvent vapors in NP films as a function of PFOT: DDT mixed ligand shell composition. (a) 1,4-Difluorobenzene, (b) 1,3,5-trifluorobenzene. (c) 1.2.4.5-tetrafluorobenzene. and (d) hexafluorobenzene.

solves-like argument, the 0F sample exhibited more uptake of benzene than the 100F, whereas the 100F exhibited more uptake of highly fluorinated (low Hildebrand parameter) benzene derivatives (Fig. 10). These results are consistent with ESR measurements performed on fluorinated mixed ligand

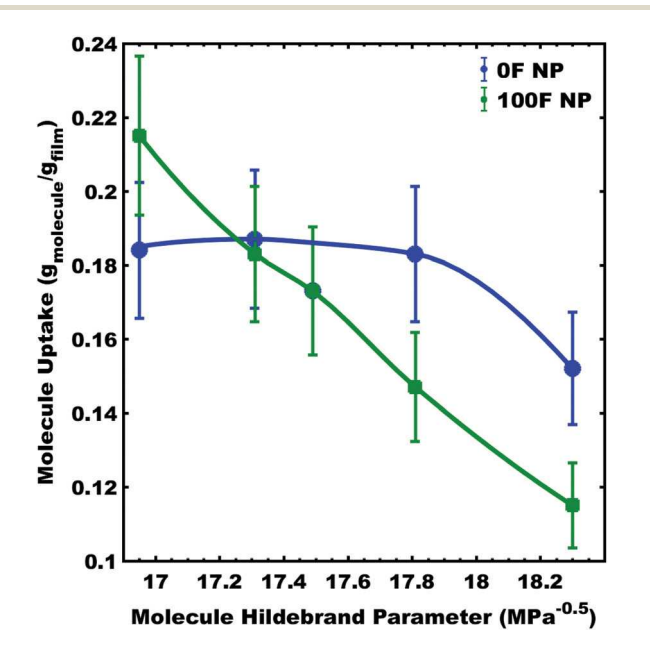


Fig. 10 Comparison of different benzene derivative uptakes into the OF and 100F NP films. The Hildebrand solubility parameter for each benzene derivative is used for the x-axis. Comparisons of 0F and 100F NP films are implied, whereas comparisons between particular molecules also include changing vapor pressure.

NPs in which the monolayers had much stronger binding affinity to highly fluorinated probes compared to the nonfluorinated counterpart. 52 The favorable interaction of PFOT with fluorinated benzene derivatives may be due to either a reduced difference in relative polarizability (dispersion forces) or possibly the presence of weak halogen bonding. Other studies have shown that weakly attractive interactions exist between fluorinated alkanes and electron deficient aromatics.53,54 QCM thus quantifies non-monotonic trends for molecule-NP interactions that are influenced by possible contributions from size/shape, ligand morphology, and chemical nature. This QCM methodology will enables future studies of structure-property relationships for molecule interactions with mixed ligand NPs. This capability is crucial to support further investigations into the molecular mechanisms.

## Conclusions

A method to quantify mixed ligand shell molecule-NP interactions was developed that is independent of solvation criteria. A QCM apparatus was used to measure the vapor phase uptake of molecules into solid NP thin films. A series of mixed ligand NPs with constant size and variable PFOT/DDT composition were prepared and were confirmed by 19F NMR to have a range of ligand shell morphologies. The NPs uptake was measured with a systematic series of fluorinated benzene derivatives. The relative mass uptake was non-monotonic with NP ligand shell composition in all cases. For the cases examined, patchy ligand morphologies were found to exhibit more molecule uptake than either stripe-like or the analogous mono-ligand NPs. This enhanced uptake was attributed to confinement effects. In contrast, stripe-like morphologies exhibited decreased molecule uptake relative to the mono-ligand NPs, consistent with cavitation effects. These results highlight the role of ligand shell morphology on molecule-NP interactions. Notably the technique enabled measurements with non-solvents. The ability to measure interactions without a solvation shell leads to a more complete understanding of molecule-NP interactions.

## Conflicts of interest

There are no conflicts to declare.

# **Acknowledgements**

Zachary Marsh and Kayla A. Lantz acknowledge support by the National Science Foundation EPSCoR Program under NSF Award #OIA-1655740. Morgan Stefik acknowledges support by the National Science Foundation (DMR-1752615). This work made use of the South Carolina SAXS Collaborative, supported by the NSF Major Research Instrumentation program (award #DMR-1428620). B. Lamm is thanked for assistance with MATLAB code. Dr Pellechia and H. Cohen are thanked for

Nanoscale Paper

assistance with NMR techniques. Dr Greytak is thanked for helpful discussions. W. van den Bergh is thanked for many analytical discussions. A. Sarkar is thanked for reaction discussions. A. Pingitore is thanked for help plumbing the solvent vapor apparatus.

## References

- 1 S. Eustis and M. A. El-Sayed, Chem. Soc. Rev., 2006, 35, 209-217
- 2 K. Saha, S. S. Agasti, C. Kim, X. Li and V. M. Rotello, Chem. Rev., 2012, 112, 2739-2779.
- 3 P. Ghosh, G. Han, M. De, C. K. Kim and V. M. Rotello, Adv. Drug Delivery Rev., 2008, 60, 1307-1315.
- 4 Z. Nie, A. Petukhova and E. Kumacheva, Nat. Nanotechnol., 2010, 5, 15-25.
- 5 G. Aragay, J. Pons and A. Merkoçi, Chem. Rev., 2011, 111, 3433-3458.
- 6 H. Niu, S. Wang, Z. Zhou, Y. Ma, X. Ma and Y. Cai, Anal. Chem., 2014, 86, 4170-4177.
- 7 O. Uzun, Y. Hu, A. Verma, S. Chen, A. Centrone and F. Stellacci, Chem. Commun., 2008, 196-198.
- 8 S. Bidoggia, F. Milocco, S. Polizzi, P. Canton, A. Saccani, B. Sanavio, S. Krol, F. Stellacci, P. Pengo and L. Pasquato, Bioconjugate Chem., 2017, 28, 43-52.
- 9 S. J. Stranick, A. N. Parikh, Y. T. Tao, D. L. Allara and P. S. Weiss, J. Phys. Chem., 1994, 98, 7636-7646.
- 10 J. P. Folkers, P. E. Laibinis and G. M. Whitesides, Langmuir, 1992, 8, 1330-1341.
- 11 P. E. Laibinis, M. A. Fox, J. P. Folkers and G. M. Whitesides, Langmuir, 1991, 7, 3167-3173.
- 12 S. Imabayashi, N. Gon, T. Sasaki, D. Hobara and T. Kakiuchi, Langmuir, 1998, 14, 2348-2351.
- 13 J. J. Kuna, K. Voïtchovsky, C. Singh, H. Jiang, S. Mwenifumbo, P. K. Ghorai, M. M. Stevens, S. C. Glotzer and F. Stellacci, Nat. Mater., 2009, 8, 837-842.
- 14 I. C. Pons-Siepermann and S. C. Glotzer, ACS Nano, 2012, 6, 3919-3924.
- 15 H. Kim, R. P. Carney, J. Reguera, Q. K. Ong, X. Liu and F. Stellacci, Adv. Mater., 2012, 24, 3857–3863.
- 16 P. K. Ghorai and S. C. Glotzer, J. Phys. Chem. C, 2010, 114, 19182-19187.
- 17 A. M. Jackson, J. W. Myerson and F. Stellacci, Nat. Mater., 2004, 3, 330-336.
- 18 W. Edwards, N. Marro, G. Turner and E. R. Kay, Chem. Sci., 2017, 9, 125-133.
- 19 C. H. Rycroft, G. I. Barenblatt, K. Yamagata, T. Kondo, S. Hayashi, A. Shitamukai, D. Konno, F. Matsuzaki, S. Onami, H. Nakayama, Y. Kosugi, T. M. Watanabe,

  - K. Fujita, Y. Mimori-, M. Signaling, C. Asymmetry,
  - C. Asymmetry, K. Yamagata, T. Kondo, S. Hayashi,
  - A. Shitamukai, D. Konno, F. Matsuzaki, J. Takayama, S. Onami, H. Nakayama, Y. Kosugi, M. Tomonobu, K. Fujita and Y. Mimori-kiyosue, Proc. Natl. Acad. Sci. U. S. A., 2008, 110, 6240-6240.

- 20 M. Sologan, C. Cantarutti, S. Bidoggia, S. Polizzi, P. Pengo and L. Pasquato, Faraday Discuss., 2016, 191, 527-543.
- 21 R. Stangenberg, I. Saeed, S. L. Kuan, M. Baumgarten, T. Weil, M. Klapper and K. Müllen, Macromol. Rapid Commun., 2014, 35, 152-160.
- 22 D. Segets, J. Gradl, R. K. Taylor and V. Vassilev, ACS Nano, 2009, 3, 1703-1710.
- 23 L. V. Stebounova, E. Guio and V. H. Grassian, J. Nanopart. Res., 2011, 13, 233-244.
- 24 F. P. Zamborini, M. C. Leopold, J. F. Hicks, P. J. Kulesza, M. A. Malik and R. W. Murray, J. Am. Chem. Soc., 2002, 124, 8958-8964.
- 25 Y. Joseph, A. Peie, X. Chen, J. Michl, T. Vossmeyer and A. Yasuda, J. Phys. Chem. C, 2007, 111, 12855-12859.
- 26 J. Im, A. Chandekar and J. E. Whitten, Langmuir, 2009, 25, 4288-4292.
- 27 F. J. Ibañez and F. P. Zamborini, Small, 2012, 8, 174–202.
- 28 R. Z. Hao, H. Bin Song, G. M. Zuo, R. F. Yang, H. P. Wei, D. B. Wang, Z. Q. Cui, Z. P. Zhang, Z. X. Cheng and X. E. Zhang, Biosens. Bioelectron., 2011, 26, 3398-3404.
- 29 V. Pavlov, Y. Xiao, B. Shlyahovsky and I. Willner, J. Am. Chem. Soc., 2004, 126, 11768-11769.
- 30 Y. Ding, J. Liu, H. Wang, G. Shen and R. Yu, Biomaterials, 2007, 28, 2147-2154.
- J. Santos-Martinez, 31 A. Lesniak, A. Salvati, M. M. W. Radomski, K. A. Dawson and C. Åberg, J. Am. Chem. Soc., 2013, 135, 1438-1444.
- 32 M. Sologan, D. Marson, S. Polizzi, P. Pengo, S. Boccardo, S. Pricl, P. Posocco and L. Pasquato, ACS Nano, 2016, 10, 9316-9325.
- 33 X. Liu, M. Atwater, J. Wang and Q. Huo, Colloids Surf., B, 2007, 58, 3-7.
- 34 A. M. Smith, K. A. Johnston, S. E. Crawford, L. E. Marbella and J. E. Millstone, Analyst, 2017, 142, 11-29.
- 35 C. Singh, P. K. Ghorai, M. A. Horsch, A. M. Jackson, R. G. Larson, F. Stellacci and S. C. Glotzer, Phys. Rev. Lett., 2007, 99, 1-4.
- 36 R. P. Carney, G. A. DeVries, C. Dubois, H. Kim, Y. K. Jin, C. Singh, P. K. Ghorai, J. B. Tracy, R. L. Stiles, R. W. Murray, S. C. Glotzer and F. Stellacci, J. Am. Chem. Soc., 2008, 130, 798-799.
- 37 M. J. Hostetler, S. J. Green, J. J. Stokes and R. W. Murray, J. Am. Chem. Soc., 1996, 118, 4212-4213.
- 38 L. O. Brown and J. E. Hutchison, J. Am. Chem. Soc., 1997, 119, 12384-12385.
- 39 Z. Luo, J. Hou, L. Menin, Q. K. Ong and F. Stellacci, Angew. Chem., Int. Ed., 2017, 56, 13521-13525.
- 40 N. R. Jana and X. Peng, J. Am. Chem. Soc., 2003, 125, 14280-14281.
- 41 A. Dass, R. Guo, J. B. Tracy, R. Balasubramanian, A. D. Douglas and R. W. Murray, Langmuir, 2008, 24, 310-315.
- 42 T. Yonezawa, S. Y. Onoue and N. Kimizuka, Adv. Mater., 2001, 13, 140-142.
- 43 X. Liu, M. Yu, H. Kim, M. Mameli and F. Stellacci, Nat. Commun., 2012, 3, 1182-1189.

Paper

44 S. Pradhan, L. E. Brown, J. P. Konopelski and S. Chen, *J. Nanopart. Res.*, 2009, **11**, 1895–1903.

- 45 K. M. Harkness, A. Balinski, J. A. McLean and D. E. Cliffel, *Angew. Chem., Int. Ed.*, 2011, 50, 10554–10559.
- 46 Y. F. Hu, B. H. Wansch, S. Sahni and F. Stellacci, *J. Scanning Probe Microsc.*, 2009, 4, 24–35.
- 47 Y. Wang, O. Zeiri, A. Neyman, F. Stellacci and I. A. Weinstock, *ACS Nano*, 2012, **6**, 629–640.
- 48 M. Lucarini and L. Pasquato, Nanoscale, 2010, 2, 668.
- 49 A. Centrone, Y. Hu, A. M. Jackson, G. Zerbi and F. Stellacci, *Small*, 2007, **3**, 814–817.

- 50 S. Pradhan, L. P. Xu and S. Chen, *Adv. Funct. Mater.*, 2007, 17, 2385–2392.
- 51 J. A. Emerson, D. T. W. Toolan, J. R. Howse, E. M. Furst and T. H. Epps, *Macromolecules*, 2013, **46**, 6533–6540.
- 52 M. Boccalon, S. Bidoggia, F. Romano, L. Gualandi, P. Franchi, M. Lucarini, P. Pengo and L. Pasquato, *J. Mater. Chem. B*, 2015, 432–439.
- 53 S. I. Kawahara, S. Tsuzuki and T. Uchimaru, *J. Phys. Chem. A*, 2004, **108**, 6744–6749.
- 54 G. Cavallo, P. Metrangolo, R. Milani, T. Pilati, A. Priimagi, G. Resnati and G. Terraneo, *Chem. Rev.*, 2016, **116**, 2478–2601.